



Constrained crystal growth during solidification of particles and splats in uniform droplet sprays

Yiannos Ioannou¹ · Hiroki Fukuda² · Claus Rebholz³ · Yiliang Liao⁴ · Teiichi Ando⁵ · Charalabos C. Doumanidis⁶

Received: 8 October 2019 / Accepted: 12 February 2020 / Published online: 22 February 2020
© Springer-Verlag London Ltd., part of Springer Nature 2020

Abstract

Uniform droplet spraying (UDS) is a novel process used to produce ideally narrow (mono-size) distributions of molten metal droplets for various applications. The crystallite size is a primary determinant of mechanical properties in solidified alloy deposits and thus in need of predictive modeling. This project reports on employing UDS as a paradigm for solidification modeling of mono-size solid droplets in an oil bath, as well as planar and globular splats on a cooling substrate, for magnesium alloys AZ91D and Mg₉₇ZnY₂. The model combines a nucleation and dendrite fragmentation description from solidification theory, with a framework for constrained growth of crystalline domains confined by adjacent developing ones. The latter is based on differential attributes of the dynamic temperature field during solidification, derived from semi-analytical expressions for the simple droplet and splat geometries above. The modeling results are validated against measured domain size distributions on section micrographs, and found to be within a – 10% to + 14% estimation error range. Further improvement of the model via numerical thermal descriptions for off-line material design and optimization in additive manufacturing is discussed, along with its use as real-time structural observer for closed-loop control based on temperature measurements in UDS-based processes.

Keywords Rapid solidification processing · Uniform droplet spraying · Constrained growth · Mg alloy splats

1 Introduction

Development of high mechanical performance alloys, e.g., through grain boundary (Hall-Petch) strengthening via dislocation motion control by grain refinement [1, 2], can be hardly overemphasized in modern technological applications. Aside from various nucleants and induced dendrite fragmentation

processes, fine-grained microstructures have been pursued via pronounced undercooling during rapid solidification processing (RSP), i.e., in gas atomization, melt spinning, spray forming, and other methods [3–5]. In these techniques, refined structures of the solid deposits are promoted by faster solidification of fine droplets of the melt. However, pyrophoricity of such metallic sprays initiated by the finer droplets in the resulting size distribution, often limits the RSP production conditions, and therefore the obtained deposit structures and alloy properties [6].

More recently, a novel uniform droplet spraying (UDS) technique was introduced to produce ideally narrow (mono-size) distributions of molten droplets [7]. UDS droplets are fine enough to induce RSP structural refinement and strengthening effects, yet without submicron and nano-sized droplet contents igniting in-process pyrophoric reactions. In the UDS, a thermostatically controlled, heated crucible containing the molten alloy under applied inert gas pressure ejects a melt jet from an orifice at its bottom. This separates into a stream of uniformly sized spherical droplets, via capillary breakup induced by a piezoelectrically vibrated transducer rod in the melt [8]. The mono-sized spray can be electrically charged to avoid droplet coalescence during their flight in a controlled

✉ Yiliang Liao
yliao@unr.edu

¹ Department of Materials Science, Montanuniversität Leoben, 8700 Leoben, Austria

² Fukuda Metal Foil & Powder Co. Ltd, Kyoto 607-8305, Japan

³ Department of Mechanical and Manufacturing Engineering, University of Cyprus, CY-1678 Nicosia, Cyprus

⁴ Department of Mechanical Engineering, University of Nevada Reno, Reno, NV 89557, USA

⁵ Department of Mechanical and Industrial Engineering, Northeastern University, Boston, MA 02115, USA

⁶ College of Engineering & Computer Science, Vin University, Hanoi, Vietnam

environment chamber. Droplets are collected at the desired precise thermal and solidification state, as perfectly spherical particles in an oil bath, or as splats and deposits on a cooled substrate [9]. The UDS method has been successfully demonstrated for a variety of metallic materials, from low-melting solders [10, 11] all the way to aluminum and ferrous alloys [12, 13]. The UDS has been suggested for scalable production via multi-orifice systems, as well as for additive manufacturing by 3D printing/welding of fully dense metal parts of arbitrary geometry from superheated droplets.

Modeling of droplet in-flight solidification during the UDS process has been established on the basis of four components: (i) a formulation of droplet motion, based on a description of the Rayleigh capillarity instability and breakup of a laminar jet under an oscillation wavelength and frequency range [14], coupled with Newtonian dynamics of motion under a gravitational field, aerodynamic drag, and electrostatic repulsion [15, 16]; (ii) a thermal model of the droplet, describing via 1st law thermodynamics its enthalpic changes through convective and radiative losses by surface heat transfer, along with volume solidification phase changes accounting for latent heat of fusion effects during recalescence [17, 18]; (iii) a free dendritic growth model of droplet solidification, based on linear [19–21] or non-linear [22] representations of the liquidus and solidus curves in a (pseudo) binary phase diagram of the alloy. This provides morphology (tip radius of a paraboloid) of the solid-liquid interface of an unconstrained dendrite, its kinetics (growth velocity) and thermal and solutal profiles across its surface as functions of undercooling; and (iv) a dendrite fragmentation model via remelting upon recalescence, driven by crystal supersaturation and/or capillary forces on the solid-liquid interface, when a modeled breakup time exceeds a plateau duration [23, 24]. Although such modeling was successfully validated for various UDS sprayed materials, including eutectic Sn-Pb- [25], Cu- [26], Cr- [27], Fe- [28], and Mg-based alloys [29], its quantitative, predictive connection to the solidified microstructure and mechanical properties remains yet to be established. One key aspect to this purpose consists in the prediction of grain size distribution in the solidified structure, resulting from constrained crystal domains growing against adjacent ones during rapid solidification.

Therefore, this article aims at theoretically proposing and experimentally testing such a constrained crystal growth model component for RSP of Mg alloys, with computational efficiency suitable for real-time implementation for UDS process control. Section 2 describes the UDS setting used in the experimental tests, the processing conditions, and alloy properties, along with the resulting microstructure image analysis. Section 3 introduces a theoretical formulation of crystallite size growth based on Arrhenius solidification kinetics and geometric confinement dependent on the local temperature distribution. The results in Section 4 compare the model

predictions with measurements of domain size in UDS-solidified products of simple geometry, including droplet spheres and flat and ellipsoidal splats on a substrate, for two Mg-based alloys. Finally, Section 5 relays a discussion on the results and their future improvement potential, while Section 6 summarizes conclusions and future work towards applicability of such grain size modeling to material optimization as well as process observation and feedback control.

2 Material and methods

The experimental UDS setting (as shown in Fig. 1) is used for RSP of Mg alloys [30]. The setup consists of the heating system, crucible, vibration transmission, gas pressurization and circulation, droplet charging, environmental chamber, droplet collection, and stroboscopic monitoring system. The heating system includes a water-cooled copper induction coil with a matching box and a high-frequency AC power control unit (Nissin-Giken), along with a chiller recirculator (NESLAB). The cylindrical crucible assembly from stainless steel includes a bottom plate and an insert with an orifice hole machined at its center, and is insulated from the coil by a quartz tube and graphite felt layer, and from the UDS chamber by alumina blocks (Fiberfrax), permitting melt temperatures up to ~ 1800 K. A wire-pull arm is used to prevent orifice clogging due to oxidation of the molten metal. The vibration assembly comprises a piezoelectric transducer disk stack (EDO) with brass spacers, screw-fastened between the top stainless steel plate via an o-ring and an aluminum plate. The piezoelectric transducer is driven by a digital function generator (BK Precision) through an AC voltage amplifier (Radio Shack), with its waveform monitored by a dual-trace oscilloscope (Leader). The transducer rod acting on the alloy melt near the orifice through a conical stainless steel tip consists of a ceramic protection tube, surrounding a K-type thermocouple (Omega) to measure the melt temperature in the crucible.

The cylindrical UDS chamber is also made of stainless steel with transparent window ports for a high-speed camera and strobe light driven by the function generator (Strobotac) for imaging of the droplets in flight (Fig. 2). Inside the chamber, a calorimetric container with a stirrer is used to collect spherical droplets in an oil bath, and a droplet quencher with substrate blades rotating at adjustable speeds and heights is employed for the collection of non-overlapping splats (Fig. 1b). Both are supported on a computer-driven motorized X-Y table through a scissor jack adjusting the droplet collection height Z. The setting is completed by a vacuum pump, an ultrahigh-purity argon tank supply and an oxygen analyzer.

Note that despite ultimate controllability in the ejected metal/alloy droplet material selection, shape, size, and thermal state, the UDS experimental equipment is quite complex. Part

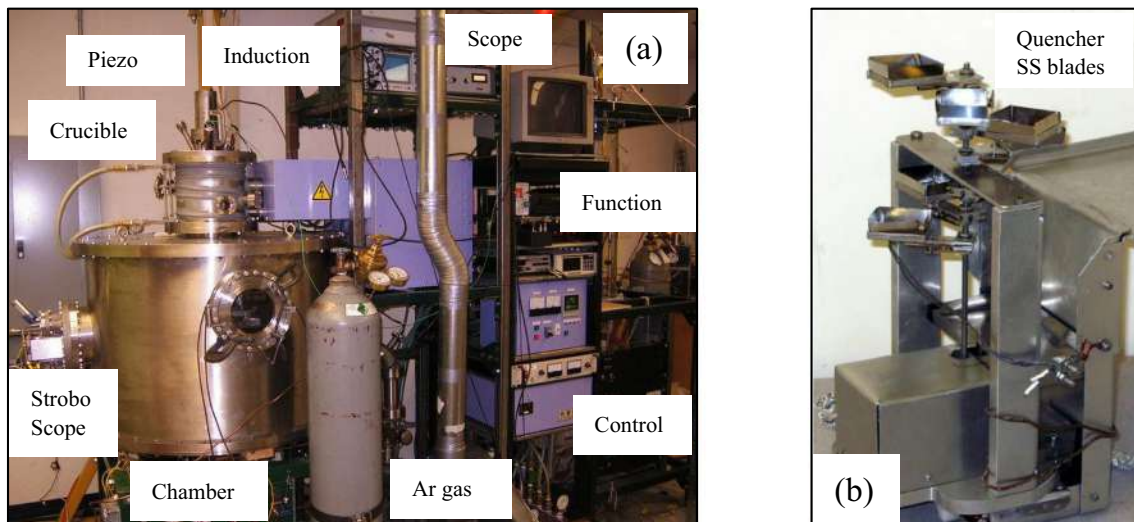


Fig. 1 **a** Uniform droplet spray setting and **b** droplet collection system, adopted with permission from [30]

of this complexity requirement arises from the enclosed deposition chamber, which needs to be purged several times by inert gas in order to reduce residual oxygen to levels that would be safe against pyrophoric ignition in case ultrafine droplets appear inadvertently. This increases the startup time of the process and the cost of equipment. Additional limitations arise from the relatively low droplet jet yield of a single-orifice setting, while multi-orifice ones are more expensive. Last, the positioning accuracy of electrostatically charged droplets impinging on the substrate decreases with flight distance, along with disturbances from stray external fields and interference effects between droplets.

In preparation for each experiment, the Mg alloy materials (AZ91D and $Mg_{97}ZnY_2$) are cut from as-cast ingots (Fukuda) into bars using a coolant to avoid ignition, and subsequently ground and polished and ultrasonically cleaned to remove oxides and impurities leading to orifice clogging. After filling the crucible, the UDS setup is cleaned with acetone,

assembled, and inspected. The chamber is repeatedly evacuated and back-filled with UHP Ar gas to a final pressure of 5 psi, with oxygen content purged to about 1 ppm. The heating system is activated under thermostatic control to the target melt temperature, the droplet collectors are properly positioned in the chamber, and the stroboscopic monitor and vibration transducer are started with a 2.4-kHz sinusoidal wave excitation for a 348- μm orifice diameter. Finally, the melt ejection is started by an inert gas over-pressure of 2 psi in the crucible, adjusted along with the vibration frequency to maintain a steady flow during the experiment, until its conclusion when the crucible melt load is depleted. Table 1 illustrates the UDS processing conditions used in the experimental tests, while Table 2 quotes the relevant material properties of the two Mg alloys employed [31].

The mono-sized spherical solid droplets and/or splats are subsequently collected from the UDS setup, ultrasonically cleaned and encapsulated for standard specimen material analysis by sectioning, polishing, and etching. Section micrographs are obtained by a metallurgical digital microscope (Olympus) at various resolutions (Fig. 3). The obtained material microstructures are analyzed for crystallite size distributions by image processing techniques based on grayscale blob segmentation and edge detection via tessellated quadtree raster methods for spatial occupancy [38] by commercial software routines (MATLAB) on standard desktop PC hardware. Each micrograph section intersects randomly oriented crystallite domains, generally consisting of independently nucleated grains, fragmented dendrite arms, and dendritic grain trunks, all grown to a spatially cohesive microstructure (Fig. 4). Such domains with 3D warped ellipsoid, cylindroid, conoid, and/or paraboloid solid geometry, as observed and modeled in the literature [19, 20, 22, 39], yield planar sections with generalized ellipsoidal connected assemblies (Figs. 3 and 4), each with half-axes u , w . At each

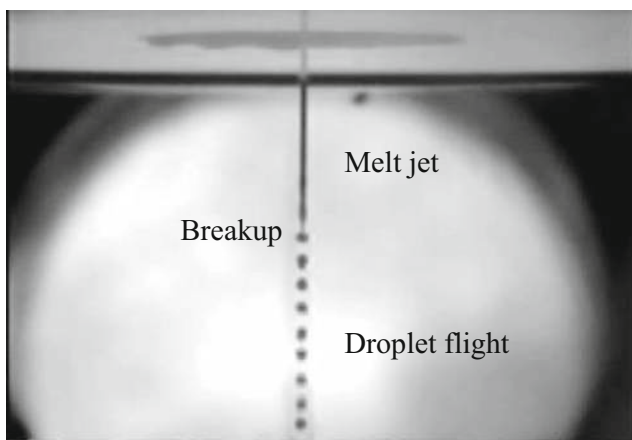


Fig. 2 Stroboscopic image of droplet flight in UDS of AZ91D alloy, adopted with permission from [30]

Table 1 UDS process conditions in experimental tests [29, 30]

Test case/process condition	Spherical droplet	Planar splat	Globular splat
Alloy material	AZ91D	Mg ₉₇ ZnY ₂	Mg ₉₇ ZnY ₂
Melt temperature (K)	973	973	973
Orifice diameter (μm)	348	348	348
Gas pressure (psi)	5	2	2
Piezo frequency (kHz)	2.39	2.39	2.39
Droplet diameter (μm)	700	700	700
Flight distance (m)	0.35	0.25	0.25
Droplet direction	Vertical	Vertical	Angled
Collection medium	Oil bath	SS substrate	SS substrate
Collect drop temp (K)	868	965	936

examined location in the micrographs, the measured planar section area A of domains, averaged over a square box centered at that target position, is employed to derive an apparent domain size S :

$$S \equiv 2\sqrt{uw} = 2\sqrt{\frac{A}{\pi}} \quad (1)$$

Thus, S represents the diameter of an equivalent circular disk with the same apparent area A as the average intersected domain, and is used accordingly below without loss of topological generality. The measurement of grain size is defined in Eq. 1, which applies to both equiaxed grains (in which case S coincides with average diameter D) and non-equiaxed ones (in which it yields an equivalent size, as shown in Fig. 3). The essence of size definition S from grain section area A is shown in Eq. 1, in which area A is well-defined by image processing via blob growing in the MATLAB on the micrographs. Note that size S in Eq. 1 is mean grain size. Effect of elemental composition segregation and solid-liquid interface deformation could have a second- or third-order effect on grain size distribution. The way size is defined via Eq. 1 makes it

Table 2 Physical properties of Mg alloys [25, 30–37]. Some values for Mg₉₇ZnY₂ alloy unavailable in the literature are approximately estimated by projection in pseudo-binary phase diagrams, or by calculation via the law of mixtures from data in the references

Alloy material/property	AZ91D	Mg ₉₇ ZnY ₂
Liquidus temperature T_L (K)	868	903
Solidus temperature T_S (K)	743	713
Latent heat of fusion Δh (kJ/kg)	373	362
Liquid density ρ_L (g/cm ³)	1.65	1.68
Solid density ρ_S (g/cm ³)	1.81	1.85
Heat capacity c (kJ/kgK)	1.047	1.026
Thermal conductivity k (W/mK)	72.3	64
Thermal diffusivity α (mm ² /s)	39.9	35.4

insensitive to local boundary effects. The phenomena of elemental composition segregation and solid-liquid interface deformation will be addressed in another effort, and reported separately.

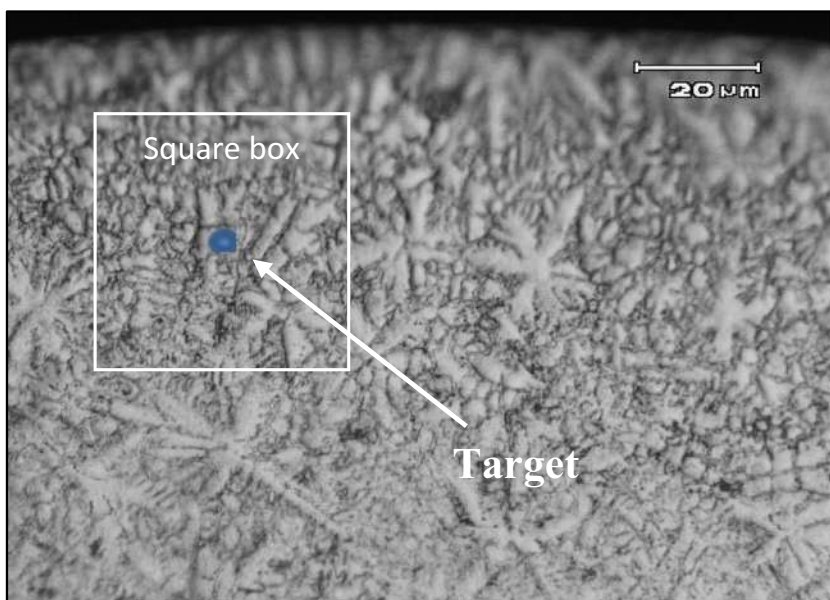
3 Theory/calculation

3.1 Nucleation and fragmentation

For quantitative prediction of such solidified crystalline domain sizes, classical solidification theory-based models for grain nucleation, dendrite fragmentation, and free growth are to be combined with a geometric confinement formulation for RSP alloys. To this end, the molten alloy, e.g., of the UDS droplets at the proper flight height, is assumed at an initial sufficiently superheated state above the liquidus temperature T_L to ensure presence of liquid phase only (i.e. no solid fraction) upon initiation of solidification. The melt is also assumed homogeneous and isotropic, without directional dependence of diffusion and conduction behavior in both the liquid and solid phases. Thermal non-equilibrium is assumed at solidification temperature T_m , i.e., at undercooling $\Delta T = T_L - T_m$. For computational efficiency, the analysis below ignores dependence of material properties on local variations of their elemental composition (i.e., concentration profiles) during solidification, as well as on temperature T , including Marangoni effects [40].

In general, under such conditions, prevalent heterogeneous nucleation in the volume V of a melt with nucleants, or at the boundary with its container surface, is described by classical nucleation theory [41]. Because of a differential in the molar Gibbs free energy ΔG between the liquid and solid phases reaching a critical value ΔG^* , nuclei of critical radius r^* are developed. According to nucleation formulations [27], the average distance L between adjacent nuclei can be determined from the volumetric nucleation rate \dot{N} as:

Fig. 3 Image analysis of UDS-processed Mg₉₇ZnY₂ splat micrograph, adopted with permission from [30]



$$L = \sqrt[3]{\frac{V}{N}} = \sqrt[3]{\frac{BV}{N}} = \sqrt[3]{\frac{BV}{N_o} \exp\left(-\frac{\Delta G^* + \Delta Q_d}{3RT}\right)}$$

$$= L_o \exp\left(-\frac{C}{T \Delta T^2} - \frac{\Delta Q_d}{3RT}\right) \tag{2}$$

$$r^* = \frac{2 \gamma_{SL}}{\Delta G} = \left(\frac{2 \gamma_{SL} T_m}{\Delta H}\right) \frac{1}{\Delta T} \text{ and } C$$

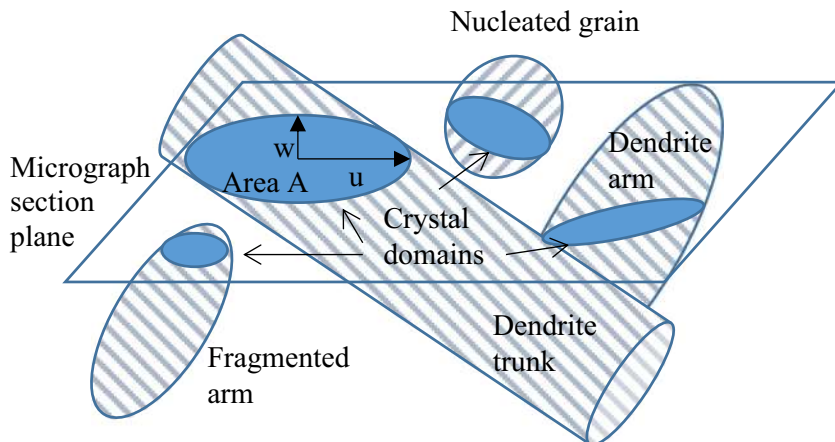
$$= \left(\frac{16\pi \gamma_{SL}^3 T_m}{9R \Delta H^2}\right) \left[\frac{(2 + \cos\theta)(1 - \cos\theta)^2}{4}\right] \tag{3}$$

where R is the universal gas constant, ΔQ_d is the molar activation energy for diffusion through the melt, N is the population of nuclei in liquid volume V , N_o is the nucleation rate constant, and $B = \dot{N}/N$ is the fractional rate of their re-dissolution into the melt at steady state. ΔH is the molar latent heat of fusion, and γ_{SL} is the specific interfacial energy (or

surface tension), and the wetting angle of the solid/liquid interface. The square-bracketed term in Eq. 3 is absent for homogeneous nucleation under special conditions.

Equation 2 highlights the dependence of the average inter-nuclear spacing L on melt temperature T and undercooling ΔT . At low cooling rates and undercooling, diffusion-limited solidification at higher temperatures typically produces well-developed solute dendrites out of nuclei; while at higher cooling rates and undercooling, temperature-controlled solidification generates refined thermal dendrites. In the latter case, typically encountered in RSP of metals, nucleation is limited by the Gibbs free energy barrier rather than atomic mobility in the melt, i.e., $\Delta G^* > \Delta Q_d$, and the diffusion term is usually ignored in Eq. 2 for the UDS of Mg alloys. However, nucleation densities \dot{N}/V still commonly limited to 10^{12} – $10^{15}/m^3s$ under such conditions, in combination with the small volume of fine UDS droplets and fast solidification times in RSP

Fig. 4 Schematic arrangement of microstructure planar section with apparent domains



(around 0.1 ms), reduce the number of nuclei N to very few (often only one) per droplet [27, 28]. A respective small number of dendrites has been indeed experimentally observed in Cu droplets [42], while the commensurate large distance between nuclei L can extend beyond the droplet size D (i.e., $L > D$). This projects primary dendrite arms all the way through droplet boundaries and yields epitaxial dendrite growth across splat interfaces to adjoining solidified droplets [16, 42].

Aside from nuclei, dendrite fragments can develop crystallite domains in the solidified structure at further pronounced cooling rates. Fragmentation of dendritic crystals into finer, randomly oriented crystallites has been observed in the UDS of Cr-based alloys upon cooling in helium [27], yielding subsequent growth of grain-refined dendrites. The conditions for such dendrite breakup have been established in this case by a fragmentation model [24], via the requirement that the breakup time Δt_{bu} does not exceed a fragmentation plateau duration Δt_{pi} , i.e., $\Delta t_{bu} < \Delta t_{pi}$. Such RSP conditions of higher cooling rates and undercooling lead to sharper dendrites (smaller tip and trunk radii) according to the sharp-interface model for free dendrite growth [19, 20, 22, 39]. These can result in fragmentation of dendritic arms and a refined microstructure of equiaxed dendrites, such as the starfish grains in Fig. 3 for the UDS of Mg alloys, even for limited potency ΔG and population N of nucleants. Dendrite fragmentation is triggered by recalescence causing local arm re-melting and supersaturation, along with capillary forces at the solid-liquid interface [24]. Such dendrite breakup is driven by thermal activation over a Gibbs free energy barrier (similar to ΔG^* , Eq. 2) for a melting phase change involving latent heat (i.e., ΔH) and solid-liquid surface tension effects (γ_{SL} , Eq. 3), along with elemental diffusion (ΔQ_d , Eq. 2), to cause fragmentation at a critical dendrite size (similar to r^* , Eq. 3). Therefore, because of thermo-kinetic analogy with nucleation, fragmentation is assumed below to initiate growing grains out of breakup arms similarly to nucleants above, at a dendrite arm spacing described analogously to L in Eq. 2, with properly adjusted physical parameters.

3.2 Crystallite growth

Subsequent free grain growth in the melt assumes directional isotropy and ignores deformation of the grain solid/liquid interface into oblate paraboloids and dendritic patterns, e.g., through Mullins-Sekerka instabilities [39, 43]. This temporary conjecture of radial growth of nuclei and dendrite fragments to 3D spherical or 2D cylindrical crystal domains, as mentioned above, is without loss of generality, as it is relaxed via the definition of equivalent domain size s for the generalized ellipsoidal assemblies of experimental micrograph sections. While growth of each domain is not geometrically confined by that of adjacent ones, thermally activated, diffusion-limited growth velocity of its solid/liquid boundary, v , can be described by an Arrhenius rate equation as [44]:

$$v = v_0 \exp\left(-\frac{\Delta Q_d}{RT}\right) = \frac{dr}{dt} \quad \text{and} \quad r(t) = r^* + \int_0^t v_0 \exp\left(-\frac{\Delta Q_d}{RT(\tau)}\right) d\tau \quad (4)$$

$$\dot{v} = 4\pi r^2 v \quad \text{and} \quad v(t) = v^* + \int_0^t 4\pi r^2(\tau) v(\tau) d\tau = \frac{4}{3} \pi r^3(t) \quad \text{with} \quad v^* = \frac{4}{3} \pi r^{*3} \quad (5)$$

where r is the radius and v the volume of the solidifying crystal domain.

When domain growth takes place in the presence of other neighboring ones (also expanding), the motion of their solid/liquid interfaces is geometrically confined by each other. It is assumed below that this motion of local domain boundaries is significantly faster than the motion of the collective solidification front in the melt. Figure 5 illustrates two such adjacent spherical domains 1 and 2 at distance L , growing at average velocities v_1 and v_2 respectively because of their different average temperatures T_1 and T_2 during local solidification. The distance l between their solid/liquid interfaces diminishes until the two boundaries meet after time τ .

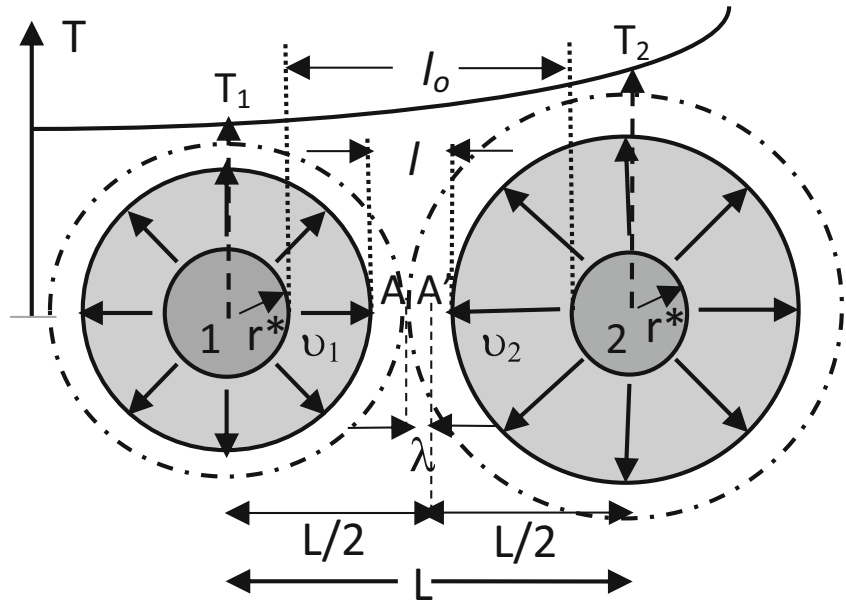
$$l(t) = l_0 - (v_1 + v_2)t \quad \text{with} \quad l_0 = L - r_1(0) - r_2(0) = bL \quad \text{and} \quad \tau = \frac{l_0}{v_1 + v_2} = \frac{bL}{2v_0} \exp\left(\frac{\Delta Q_d}{RT}\right) \quad (6)$$

$$\text{since} \quad v_1 + v_2 = v_0 \left[\exp\left(-\frac{\Delta Q_d}{RT_1}\right) + \exp\left(-\frac{\Delta Q_d}{RT_2}\right) \right] = 2v_0 \exp\left(-\frac{\Delta Q_d}{RT}\right) \quad \text{with} \quad T \approx \frac{T_1 + T_2}{2} \quad (7)$$

For illustration purposes, consider the temporary conjecture as in Fig. 5 that domain growth out of nuclei or dendrite arms 1 and 2 starts simultaneously in time, i.e., $r_1(0) = r_2(0) = r^*$, and also that the critical initial radius r^* is considerably smaller than inter-domain distance L , i.e., $r^* \ll L$ and thus $l_0 = L - 2r^* \approx L$ ($b \approx 1$). If the temperature distribution T was uniform ($DT = T_2 - T_1 = 0$), then according to Eq. 4, the growth velocities v of the two domains would be equal ($Dv = v_2 - v_1 = 0$). This would result in symmetric expansion of the domains, with their boundaries eventually meeting at point A' (Fig. 5), yielding eventually equal domain radii $r = L/2$. In the case of non-uniform T and therefore v , the resulting final displacement λ of the contact point A of the solid/liquid boundaries with respect to point A' would be:

$$\lambda = \frac{v_1 - v_2}{2} \tau = -\frac{\tau}{2} Dv \quad \text{where} \quad Dv \approx \frac{dv}{dT} DT = \frac{v_0 \Delta Q_d}{RT^2} \exp\left(-\frac{\Delta Q_d}{RT}\right) DT \quad \text{and thus} \quad (8)$$

Fig. 5 Initiation and growth of two adjacent crystal domains during solidification



$$\lambda = -\frac{bL\Delta Q_d}{4RT^2}DT \text{ or equivalently } \frac{\lambda}{L} = -\frac{b}{4RT^2}\Delta Q_d DT \approx -\frac{bL}{4RT^2}\Delta Q_d \left(\frac{dT}{dx}\right) \tag{9}$$

Therefore, for a certain crystal (e.g., middle domain in Fig. 6) confined in dimension x by two adjacent domains at average distances L , expansion of its size D is due because of the difference in displacements λ, λ' of the boundaries at its two sides:

$$\frac{D\lambda_x}{L} \approx \frac{\partial}{\partial x} \left[-\frac{bL\Delta Q_d}{4RT^2} \left(\frac{\partial T}{\partial x}\right) \right] L = -\frac{bL^2\Delta Q_d}{4R} \frac{\partial}{\partial x} \left[\frac{1}{T^2(x)} \left(\frac{\partial T(x)}{\partial x}\right) \right] = \frac{bL^2\Delta Q_d}{4RT^2} \left[\frac{2}{T} \left(\frac{\partial T}{\partial x}\right)^2 - \frac{\partial^2 T}{\partial x^2} \right] \tag{10}$$

The conjecture on simultaneous domain growth in time is now relaxed, by considering the other end case, whereby one of the domains in Fig. 5 starts expanding when the other has already fully grown, with its boundary already touching the first nucleus or fragment, i.e., $r_1(0) + r_2(0) = L$ and $l_0 = 0$ ($b = 0$). By assuming a uniform probability density function for factor b in the range (0..1), an average value $b = 1/2$ is used below. For a 3D temperature distribution around a point nucleus, or equivalently a 2D field around a linear dendrite arm, similar confined domain growth takes place in the other relevant dimensions ($y; z$) as well. Therefore, the percentile volumetric expansion of, e.g., a 3D domain Dv with respect to a corresponding original liquid volume $v_0 = V/N = L^3$ is as follows:

$$\frac{Dv}{v_0} \approx \frac{D\lambda_x}{L} + \frac{D\lambda_y}{L} + \frac{D\lambda_z}{L} = \frac{L^2\Delta Q_d}{8RT^2} \left[\frac{2}{T} (\nabla T)^2 - \nabla^2 T \right] = \frac{L^2\Delta Q_d}{8RT^2} \left[\frac{2}{k^2 T} |\vec{q}|^2 + \frac{\dot{T}}{\alpha} - \frac{\Delta h}{k} \right] \tag{11}$$

$$\vec{q} = -k\nabla T, \quad \rho c \dot{T} = -k\nabla^2 T + \Delta h, \quad \alpha = k/\rho c \tag{12}$$

where (\approx) signs above denote first-order Taylor series approximation. \vec{q} is the local heat flux, Δh is the volumetric latent

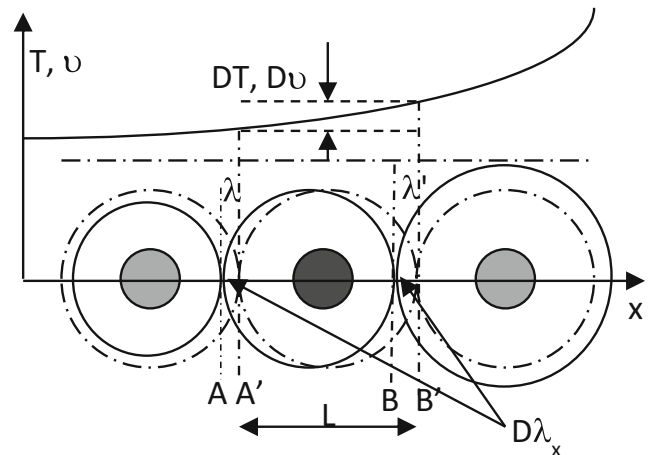


Fig. 6 Constrained domain growth by two adjacent ones in the x -dimension

heat of fusion (i.e., $\Delta h = \Delta H/\nu_m$, with ν_m the molar volume), ρ is the density, c is the specific heat capacity, k is the conductivity, and α is the thermal diffusivity of the solidifying material, with averaged values between those for liquid (at T_L) and solid (at T_S) metal, e.g., $\rho = (\rho_L + \rho_S)/2$. The bracketed part in the last term of Eq. 11 accounts for the influence of volumetric heat generation in solidification during recalescence, and the surface boundary conditions of convection in the oil bath and radiation to the UDS chamber, as well as conduction to the cooling substrate, such as:

$$q = h_a(T - T_a) + \varepsilon\sigma(T^4 - T_a^4) \quad \text{or} \quad q = -k_s \frac{\partial T_s}{\partial S} \quad (13)$$

with T_a is the ambient temperature, h_a is the convective heat transfer coefficient, ε is the surface emissivity, σ is the Stefan-Boltzmann constant, T_s is the substrate temperature, and k_s is its conductivity.

3.3 Domain size

Therefore by combining with nucleation and/or fragmentation Eq. 2, the eventual volume v of a solidified domain under constrained growth conditions can be determined from the dynamic temperature distribution operator of Eq. 11. This operator is applicable at the local solidification temperature $T = (T_L + T_S)/2 \equiv T_m$, assuming a uniform probability density function for transformation temperature T in the range $(T_S..T_L)$ at various locations of the droplet. Further, undercooling is assumed proportional to the local cooling rate at solidification, i.e., $\Delta T = \beta\tau\dot{T}$. Thus:

$$v \approx v_o \left\{ 1 + \frac{Dv}{v_o} \right\} = D \exp\left(-\frac{E}{T T^2}\right) \left\{ 1 + F \left[\frac{2}{T} (\nabla T)^2 - \nabla^2 T \right] \right\} \Big|_{T_m} \quad (14)$$

$$\text{where } D = L_o^3/\eta = \frac{BV}{\eta N_o}, E = 3C/(\beta\tau)^2, F = L^2 \Delta Q_d / 8RT_m^2 \quad (15)$$

with normalization factor η enforcing the mass conservation condition during solidification:

$$\rho_L V = \rho_S \int v dv \Rightarrow \eta = \frac{\rho_S L_o^3}{\rho_L V} \int v \exp\left(-\frac{E}{T T^2}\right) \left\{ 1 + F \left[\frac{2}{T} (\nabla T)^2 - \nabla^2 T \right] \right\} \Big|_{T_m} dv \quad (16)$$

Equation 14 reflects both nucleation and fragmentation effects through the exponential term, along with constrained growth through the bracketed term, to crystal domain solidification. From this domain volume v , an equivalent size s can be derived for comparison with apparent domain size S on the experimental micrographs (Eq. 1). By relaxing the conjecture of a spherical or cylindrical domains in Figs. 5 and 6, an average section area A over the domain length of size s

extending a volume $v = As$ is used with Eq. 1 for determining the apparent size s over a planar section of the domain:

$$s = 2\sqrt{\frac{A}{\pi}} = 2\sqrt{\frac{v}{\pi s}} \Rightarrow s = \sqrt[3]{\frac{4v}{\pi}} \approx 1.084 \sqrt[3]{v} \quad (17)$$

Therefore, evaluation of the local domain size distribution s via Eq. 17 requires application of the temperature operator of Eq. 14 on the dynamic thermal field. This can be accomplished numerically, or even semi-analytically in the case of certain explicit temperature profile responses for simple UDS solidification geometries and process conditions examined below.

4 Results

Theoretical predictions of the developed model are compared against experimental measurements of apparent domain size in typical cases of UDS rapid solidification of two Mg alloys: (1) AZ91D spherical droplets solidified in an oil bath and (2) Mg₉₇ZnY₂ flat and ellipsoidal splats solidified on a planar substrate.

4.1 Spherical droplet

For the first case of AZ91D spherical droplets solidified in an oil bath, the UDS processing conditions and the material properties are given in Tables 1 and 2, respectively. The micrograph in Fig. 7 shows the structure on a typical diametrical section of a solid droplet used in image analysis for apparent

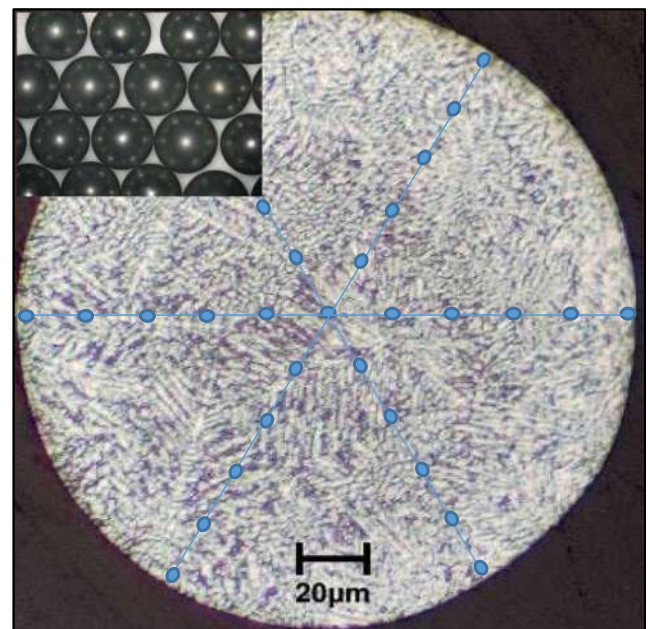


Fig. 7 Micrograph of UDS AZ91D 200- μ m solid droplet. Insert: AZ91D droplets (1 mm), adopted with permission from [29]

domain size S [29]. For comparison with the predicted size s of Eq. 17, a modified analytical solution for the dynamic temperature field T during linear thermal conduction in a solid sphere of radius R , cooling down from a uniform superheated temperature T_o through its external surface to a medium of ambient temperature T_a , is employed in Eqs. 11 and 14 [37]:

$$T(r, t) = T_a + 2(T_o - T_a) \sum_{i=1}^{\infty} (-1)^{i-1} \frac{R}{i\pi\delta r} \sin\left(\frac{i\pi\delta r}{R}\right) \exp\left[-\alpha t \left(\frac{i\pi}{R}\right)^2\right] \tag{18}$$

where the coefficient δ is used to match the convective boundary condition on the spherical surface:

$$-k \frac{\partial T}{\partial r}(R, t) = h_a(T(R, t) - T_a) \tag{19}$$

The differential terms in Eqs. 11 and 14 can be determined from Eq. 18 as:

$$\frac{\partial T}{\partial r}(r, t) = 2(T_o - T_a) \sum_{i=1}^{\infty} (-1)^{i-1} \left[\frac{1}{r} \cos\left(\frac{i\pi\delta r}{R}\right) - \frac{R}{i\pi\delta r^2} \sin\left(\frac{i\pi\delta r}{R}\right) \right] \exp\left[-\alpha t \left(\frac{i\pi}{R}\right)^2\right] \tag{20a}$$

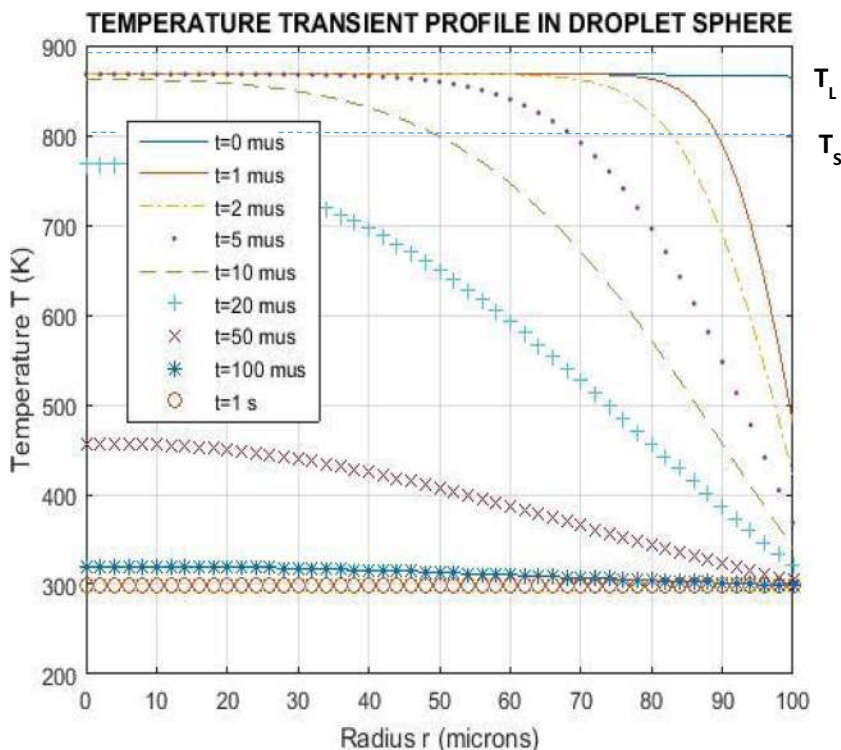
$$\frac{\partial^2 T}{\partial r^2}(r, t) = 2(T_o - T_a) \sum_{i=1}^{\infty} (-1)^i \left\{ \frac{2}{r} \left[\frac{1}{r} \cos\left(\frac{i\pi\delta r}{R}\right) - \frac{R}{i\pi\delta r^2} \sin\left(\frac{i\pi\delta r}{R}\right) \right] + \frac{i\pi\delta}{Rr} \sin\left(\frac{i\pi\delta r}{R}\right) \right\} \exp\left[-\alpha t \left(\frac{i\pi}{R}\right)^2\right] \tag{20b}$$

$$\frac{\partial T}{\partial t}(r, t) = 2(T_o - T_a) \sum_{i=1}^{\infty} (-1)^i \frac{\alpha i\pi}{R\delta r} \sin\left(\frac{i\pi\delta r}{R}\right) \exp\left[-\alpha t \left(\frac{i\pi}{R}\right)^2\right] \tag{21}$$

Figure 8 plots the temperature profiles $T(r)$ in the cooling droplet for various times t , as computed from Eq. 18 with $\delta =$

0.96. Short-time curves (for $t < 0.1 \mu s$) are plotted as needed by grain growth theory (Eq. 16), while for longer times ($t \geq$

Fig. 8 Conduction temperature profile $T(r)$ in surface-cooled sphere for various times t



0.1 ms), the predicted low radial temperature gradients ($dT/dr \sim 0.02$ K/ μm) are consistent with calculations in the literature for small Biot numbers ($Bi < 0.01$) [37]. These are employed for calculation of constrained domain size s (Eq. 17), with the coefficients in Eqs. 14, 15, and 16 adjusted at $D = 9.55 \cdot 10^{-18} \text{ m}^3$, $E = 183 \cdot 10^{15} \text{ K}^3/\text{s}^2$, and $F = 109 \cdot 10^{-18} \text{ m}^2/\text{K}$ for best fit of to the experimental data. The resulting theoretical estimates are compared against experimental values S of apparent domain size (Eq. 1) in Fig. 9. The latter are determined at target points at radial distances incremented by $20 \mu\text{m}$ from the center to the surface of the droplet, and aligned on six radii oriented every 60° from the horizontal in the micrograph of Fig. 7. The measurements are averaged over a $20 \times 20\text{-}\mu\text{m}$ square box surrounding each internal target point, while those on the perimeter part of the box area are necessarily used.

4.2 Planar splat

In the second case of $\text{Mg}_{97}\text{ZnY}_2$ flat splat solidified on a planar substrate, a superheated $\text{Mg}_{97}\text{ZnY}_2$ droplet, with UDS process conditions and material properties shown in Tables 1 and 2, respectively, collides vertically with a stainless steel cooling substrate, forming a splat disk with relatively uniform thickness in its central part [30]. Figure 10 shows the microstructure of a radial section near the center of the deposited splat, used for measurement of apparent domain

size S . Prediction of constrained growth to size s is based again on a modified analytical solution of temperature T developed by linear conduction in a planar slab of thickness d , cooled from a uniform superheated initial state T_o , through solid conduction to a flat substrate on its lower side, as well as inert gas convection and radiation to ambient temperature T_a in the chamber on its upper side, expressed as [45]:

$$T(z, t) = T_a + \frac{4}{\pi} (T_o - T_a) \sum_{i=0}^{\infty} \frac{1}{2i+1} \sin\left(\frac{(2i+1)\pi(z+\zeta)}{2d\epsilon}\right) \exp\left[-\alpha t \left(\frac{i\pi}{2d\epsilon}\right)^2\right] \quad (22)$$

where parameters ϵ and ζ are employed to match the boundary conditions on the two slab surfaces:

$$k \frac{\partial T}{\partial z}(0, t) = k_s \frac{\partial T_s}{\partial z}(0, t) \quad \text{and} \quad k \frac{\partial T}{\partial z}(d, t) = h_a(T(d, t) - T_a) + \epsilon\sigma(T^4(d, t) - T_a^4) \quad (23)$$

The differential terms in Eqs. 11 and 14 can also be determined from Eq. 22 as:

$$\frac{\partial T}{\partial z}(z, t) = \frac{2}{d\epsilon} (T_o - T_a) \sum_{i=0}^{\infty} \cos\left(\frac{(2i+1)\pi(z+\zeta)}{2d\epsilon}\right) \exp\left[-\alpha t \left(\frac{i\pi}{2d\epsilon}\right)^2\right] \quad (24)$$

$$\frac{\partial^2 T}{\partial z^2}(z, t) = -\frac{\pi}{(d\epsilon)^2} (T_o - T_a) \sum_{i=0}^{\infty} (2i+1) \sin\left(\frac{(2i+1)\pi(z+\zeta)}{2d\epsilon}\right) \exp\left[-\alpha t \left(\frac{i\pi}{2d\epsilon}\right)^2\right] \quad (25)$$

$$\frac{\partial T}{\partial t}(z, t) = -\frac{4}{\pi} (T_o - T_a) \sum_{i=0}^{\infty} \frac{\alpha}{2i+1} \left(\frac{i\pi}{2d\epsilon}\right)^2 \sin\left(\frac{(2i+1)\pi(z+\zeta)}{2d\epsilon}\right) \exp\left[-\alpha t \left(\frac{i\pi}{2d\epsilon}\right)^2\right] \quad (26)$$

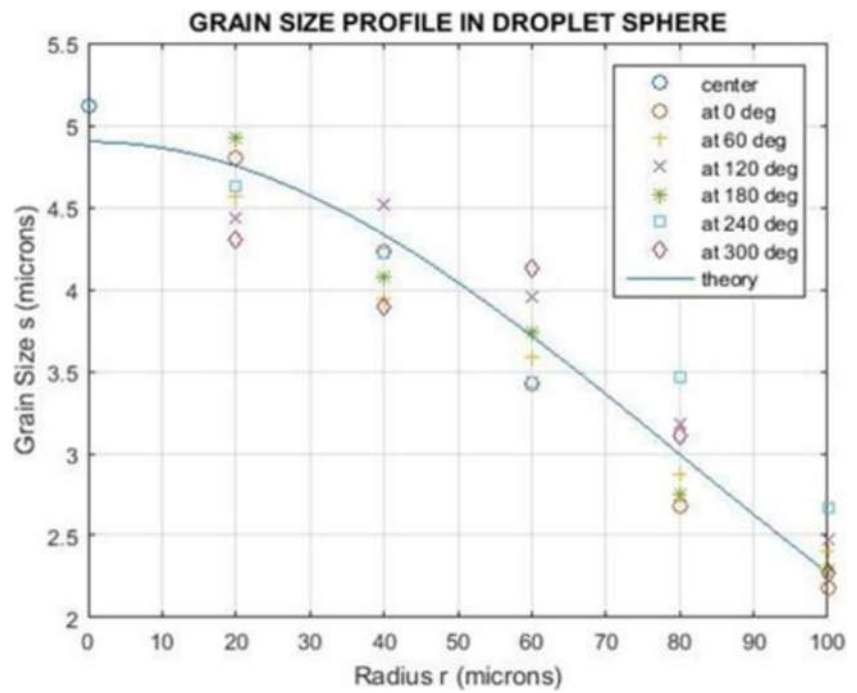
The temperature profiles $T(z)$ across the splat slab are plotted in Fig. 11 for various times t , using Eq. 22 with $\epsilon = 0.62$ and $\zeta = 2 \mu\text{m}$. Constrained growth analysis (Eqs. 11 and 14) is applied with coefficients $D = 3.74 \cdot 10^{-18} \text{ m}^3$, $E = 1.42 \cdot 10^{15} \text{ K}^3/\text{s}^2$, and $F = 24 \cdot 10^{-18} \text{ m}^2/\text{K}$ adjusted to fit the experimental data. Theoretically estimated domain sizes s are therefore computed via Eq. 17 for comparison with experimental measurements S of apparent size by Eq. 1 in Fig. 12. These are evaluated at target heights z incremented by $9 \mu\text{m}$ from the substrate lower surface towards the free top surface of the splat, along five vertical lines spaced $10 \mu\text{m}$ apart from each

other in the radial (or horizontal y) direction in the micrograph of Fig. 10. Measured domain sizes are averaged over a $10 \times 10\text{-}\mu\text{m}$ square box around each internal target, while only part of the box is employed for surface points.

4.3 Globular splat

In the third case of $\text{Mg}_{97}\text{ZnY}_2$ globular splat solidified on a planar substrate, $\text{Mg}_{97}\text{ZnY}_2$ droplet produced at the same UDS conditions as above is collected at an angle to the vertical direction on the substrate and forms a globular splat with a

Fig. 9 Crystallite domain size profile $S(r)$ in oil-quenched AZ91D spherical droplet



semi-ellipsoidal section across its diameter, as in Fig. 13 [30]. Unlike the two previous cases with a 1D heat flow and structural profile, this ellipsoidal splat entails a 2D temperature field and domain size distribution, i.e., along the radial y and elevation angle (or equivalently height z) directions from its center on the substrate boundary. An approximate product

solution for the thermal field T [45], again for linear internal conduction from a uniform initial temperature T_o , through cooling by a planar solid substrate on the lower flat boundary, and convective and radiative heat loss from its ellipsoidal free upper surface at ambient temperature T_a , is determined as:

$$T(y, z, t) = T_a + \frac{4}{\pi} (T_o - T_a) \frac{y+r}{R} \sum_{i=0}^{\infty} \frac{1}{2i+1} \sin\left(\frac{(2i+1)\pi(y+\zeta)}{2(y+r)\epsilon}\right) \exp\left[-\alpha t \left(\frac{i\pi}{2(y+r)\epsilon}\right)^2\right] \quad (27)$$

Fig. 10 Micrograph of UDS $Mg_{97}ZnY_2$ planar splat. Insert: micrograph location in planar splat, adopted with permission from [30]

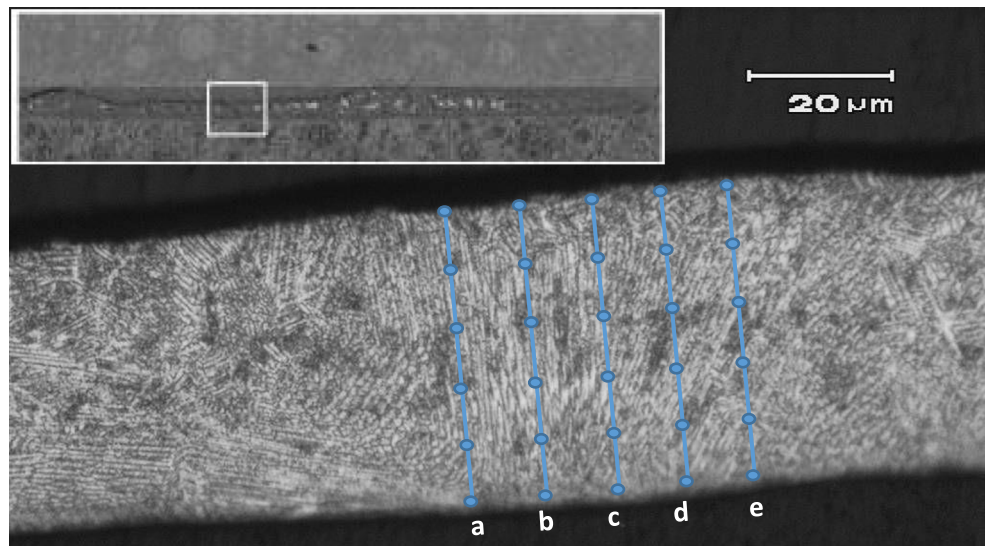
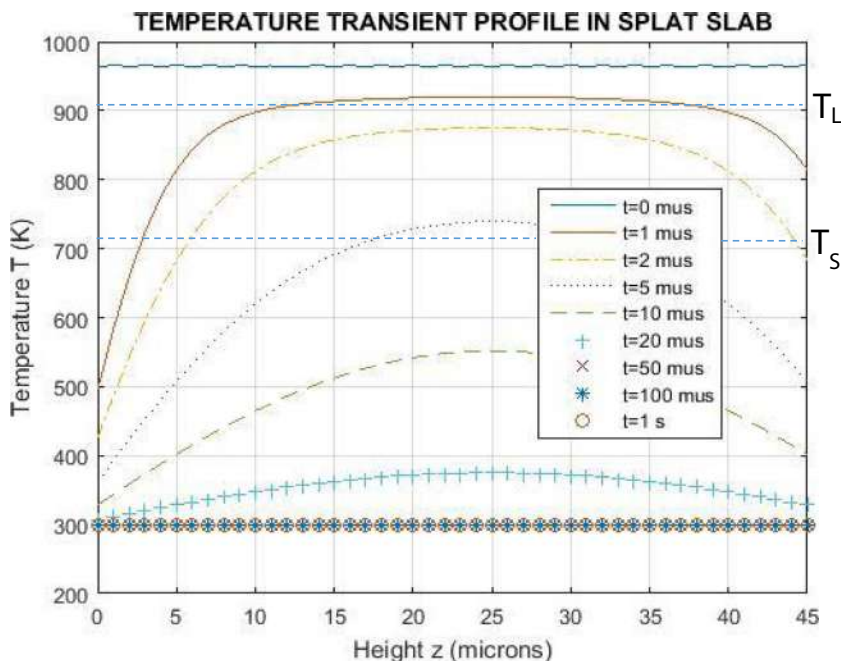


Fig. 11 Conduction temperature profile $T(z)$ in surface-cooled flat slab for various times t



$$\text{where } R = \sqrt{\frac{y^2 + z^2}{\frac{y^2}{f^2} + \frac{z^2}{g^2}}} \text{ and } r = R - \sqrt{y^2 + z^2} \quad (28)$$

and f and g are the half-axes of the ellipsoidal profile in the y and z directions, respectively, and the parameters $\epsilon = 0.7$ and $\zeta = 41 \mu\text{m}$ are adjusted as before to match boundary conditions similar to those in Eq. 23 at the two splat boundaries. The resulting temperature distribution along with isotherm

contours is plotted in Fig. 14 for $t = 100 \text{ ms}$, and was found to be in agreement with a numerical thermo-fluid simulation of the temperature and velocity field in the deposited globular splat based on level set methods, within $\pm 12\%$ [46]. Based on this dynamic thermal field, the theoretical predictions of size s are computed as before, using the previous parameter values of D , E , and F derived for the flat splat above and plotted in Fig. 15. The experimental measurements of apparent domain size S are determined at target locations $100 \mu\text{m}$ apart from

Fig. 12 Crystallite domain size profile $S(z)$ in UDS-processed $\text{Mg}_{97}\text{ZnY}_2$ -solidified planar splat

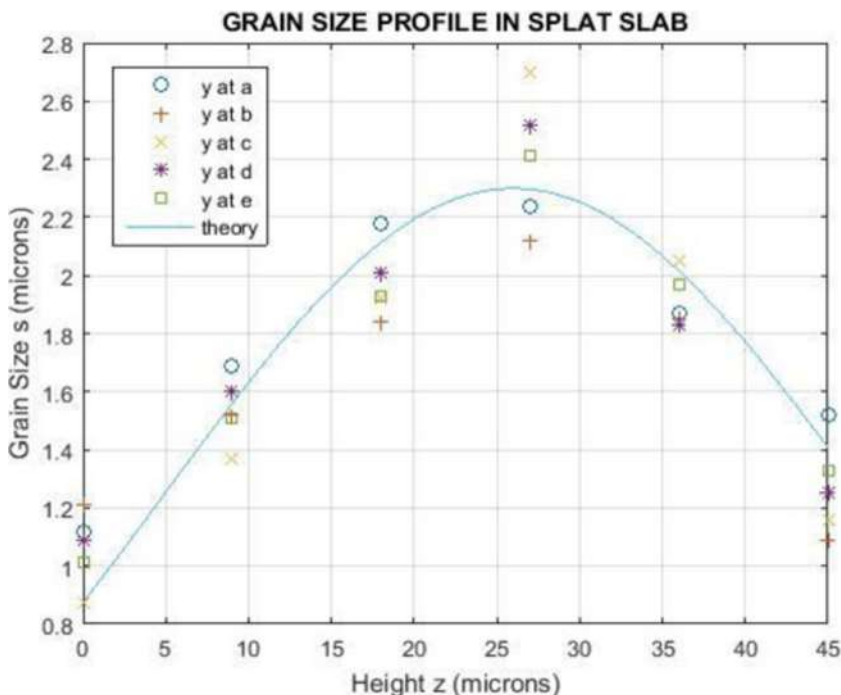
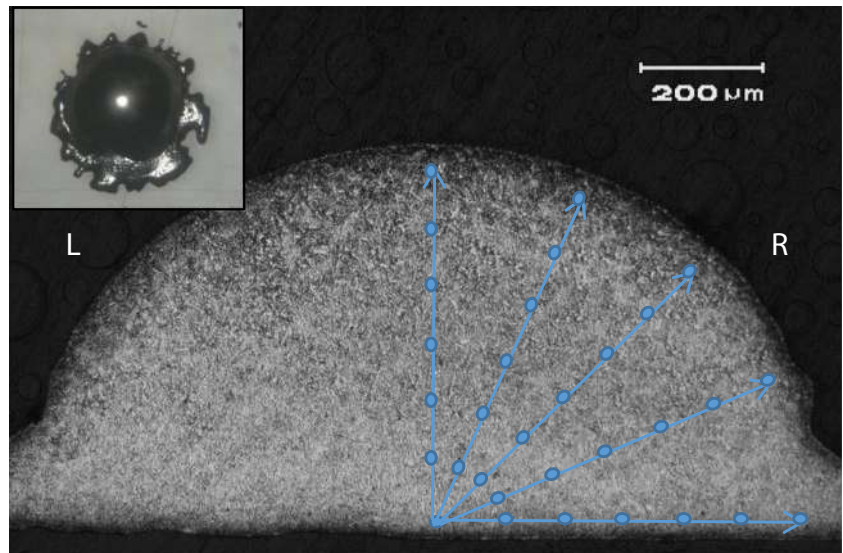


Fig. 13 Micrograph of UDS $Mg_{97}ZnY_2$ globular splat. Insert: top view of globular splat, adopted with permission from [30]



each other, along radial lines at elevation angles at 0° , 22.5° , 45° , 67.5° , and 90° with respect to the horizontal direction of the substrate boundary. Except for the vertical direction (90°), two measurements are made at the symmetrical points, in the two ellipsoidal quarters (right and left), respectively. Averaging of measured domain sizes at each position is effected over a $100 \times 100\text{-}\mu\text{m}$ square box, or part thereof its area for points near the boundaries.

5 Discussion

As expected from previous experimental reports, the UDS Mg-alloy microstructures of Figs. 7, 10, and 13 consist primarily of

α -phase Mg dendrite arms (bright areas) solidifying first. This is followed by some intergranular eutectic phase (dark interstices) richer in the alloying elements (Al and Zn in AZ91D, Zn and Y in $Mg_{97}ZnY_2$) in a pseudo-binary system of Mg with intermediary compounds (e.g., X-phase $Mg_{12}ZnY$ or I-phase Mg_3Zn_6Y in $Mg_{97}ZnY_2$ alloy) [30]. Both the RSP droplets in Fig. 7 and the splats in Figs. 10 and 13 exhibit a much finer microstructure than the original cast ingot materials, because of rapid cooling promoting solidification at deep undercooling conditions, suggesting dendrite arm fragmentation but slower growth rates of the dendrites. Average domain sizes are finer in the planar splat of Fig. 10 because of its smallest deposit thickness ($\sim 45\ \mu\text{m}$), followed by the solid droplet diameter in Fig. 7 ($\sim 200\ \mu\text{m}$) and that of the globular splat of Fig. 13 ($\sim 620\ \mu\text{m}$),

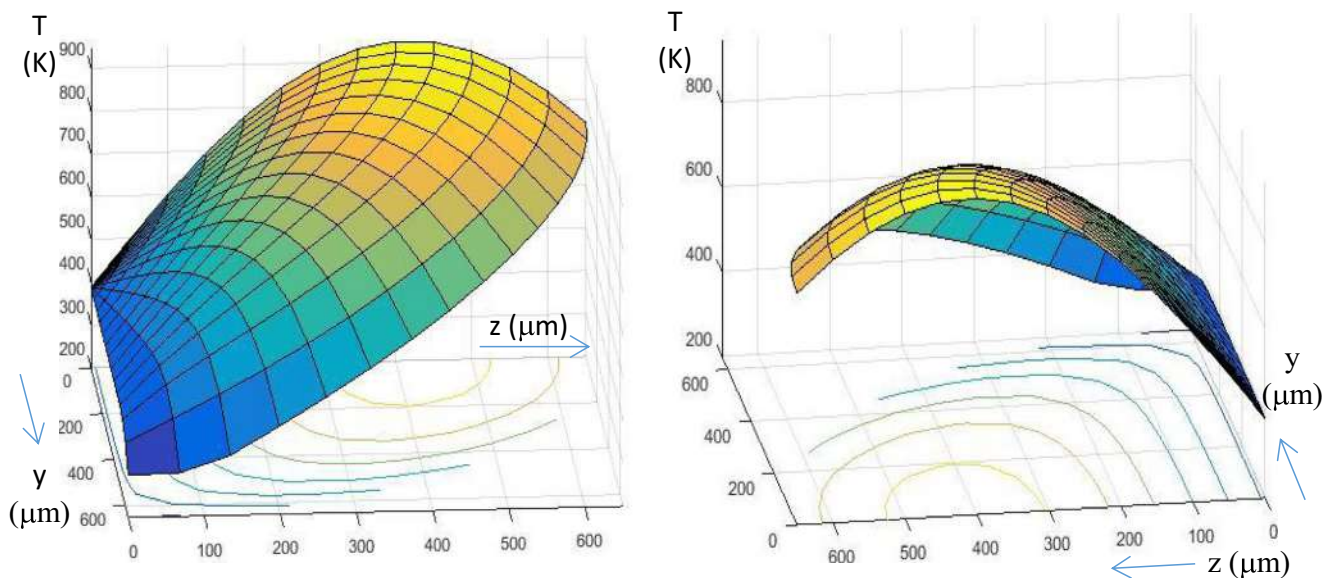
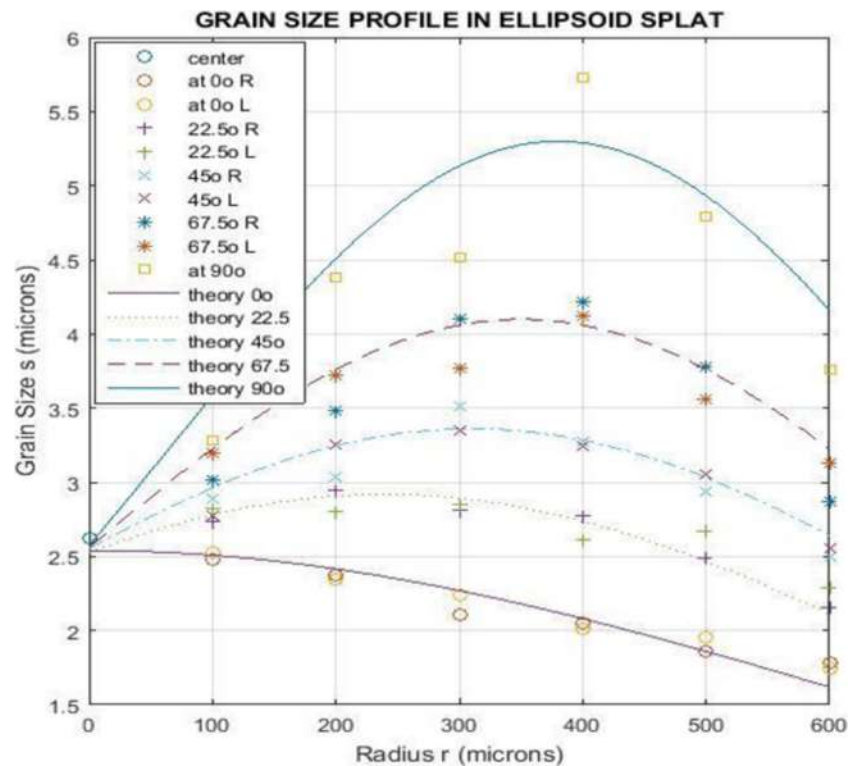


Fig. 14 Conduction temperature profile $T(y, z)$ in surface-cooled flat slab for $t = 100\ \text{ms}$

Fig. 15 Crystallite domain size profile $S(z)$ in UDS-processed $Mg_{97}ZnY_2$ -solidified planar splat



causing commensurately longer solidification times and thus decreasing rates (Figs. 9, 12, and 15).

Columnar dendritic grain structures are particularly refined and appear more equiaxed near the cooling substrate boundary of the splats (Figs. 10 and 13) due to intense conduction into the stainless steel plate of high thermal capacity, as it appears in Fig. 12 and also Fig. 15 (lower curve). This is followed by the oil bath-quenched perimeter in the spherical droplet (Fig. 7) because of liquid convection, as shown in Fig. 9 (right side), and the free boundary of the globular splats (Fig. 13) owing to gaseous convection and radiation into the UDS chamber, illustrated in Fig. 15 (right side). In central sections of all three solid particles (Figs. 7, 10, and 13), lower undercooling hindering dendrite fragmentation and lack of external boundaries for heterogeneous nucleation promote slower initiation rates, but faster and less confined grain growth, leading to larger average domain size (left of Fig. 9, center of Figs. 12 and 15). As expected by free dendritic growth theory [19, 20, 22, 39], these conditions also favor integral dendritic structures with main orientation loosely aligning to the heat flow direction, mostly in Figs. 7 and 10. Because of the relatively small initial superheating of the UDS melt over the liquidus temperature, occasional internal solidification might have started in the droplets in-flight or early upon their deposition. Along with the main solidification front from external surface boundaries, this affects the directionality of heat flow and thus that of dendrite fragmentation and growth patterns.

The solidification model for domain size of Eqs. 11–17, with geometrically constrained growth of adjacent crystals, captures such dependencies through the product of a nucleation and dendrite fragmentation term (exponential in Eq. 14), with a growth term (bracketed in Eq. 14). An increasing cooling rate \dot{T} in this exponential (also in Eqs. 21 and 26) causes deeper undercooling and increases dendrite fragmentation along with nucleation rate and thus the number of grain initiators, also dependent on their type through parameter E (Eq. 15). This in turn decreases the volume of liquid v_0 available to each initiator for confined growth, according also to factor D (Eq. 15), and therefore the average domain size in the solidified structure. However, the local crystallite growth size at a certain position of the microstructure depends, along with the diffusion rate factor F and solidification point T_m (bracketed term of Eq. 14), also on the differential terms of local temperature distribution, as per the geometrically confined growth conditions of Fig. 6. These heat transfer terms in the square brackets of Eqs. 11 and 14 are the temperature gradient ∇T (also in Eqs. 20 and 24) reflecting heat flux at conductive, convective, or radiative boundaries and geometric constriction areas, and the divergence $\nabla^2 T$ (also Eqs. 21 and 25) reflecting local cooling or latent heating, e.g., in recalescent areas. These terms influence such confined local growth conditions, thus affecting the domain size distribution. Thus, constrained growth, through the balance of these two differential terms, may create positive or negative changes to local crystallite size with respect to dendrite fragmentation and

nucleation-dependent average values on the solid microstructure.

Comparison of the model predictions for domain size to the micrograph measurements in the simple heat transfer conditions and solidification geometries of spherical droplets (Figs. 7 and 8) and planar splats (Figs. 10 and 11) is illustrated in Figs. 9 and 12, respectively. Adjustment of model parameters (D , E , and F in Eq. 14) leads to fitting of theoretical estimates to experimental data, with certain under-prediction trends at rapidly cooled boundaries (e.g., oil bath interface in the right of Fig. 9, stainless steel substrate in the left of Fig. 12) and at slower-cooling sections (e.g., sphere center in the left of Fig. 9, inert gas surface in the right of Fig. 12). These balance domain size over-prediction trends at intermediate sections of the structure (e.g., middle-radius region in Fig. 9, middle-hill acclivity areas in Fig. 12). Both deviations are attributable to simplifying assumptions of the model, most notably material homogeneity and directional isotropy in heat transfer and solidification kinetics, along with the uniform superheated state of in-flight droplets, and the simple, semi-analytical temperature field in Eqs. 18 and 22.

Validation of the model over measured domain sizes is provided in the somewhat more complex thermal transfer and geometric conditions of the globular splat (Figs. 13 and 14), as shown on Fig. 15. The model uses the previously determined parameter values for the planar splat case, and its predictions exhibit similar trends as above. These include under-prediction of experimental domain sizes at the right corner of the splat in Fig. 12 ($\sim -10\%$, right bottom of Fig. 15) where cooling rates are highest, along with the middle-section (90°) at around $400\ \mu\text{m}$ above the substrate ($\sim -10\%$, top of Fig. 15). They also include over-predictions in the rest of the materials, such as in the middle-section at around $300\ \mu\text{m}$ above the substrate ($\sim +14\%$ in Fig. 15) as expected. This leads to a modest over-prediction of the average domain size across the micrograph by the model ($\sim 1\text{--}5\%$ in Figs. 9, 12, and 15) because of its assumptions in the initiation (exponential) part of Eq. 14. This leaves local variations of domain size estimates because of the constrained growth (bracketed) part of the model in Eq. 14, to account for the balance of $\sim \pm 10\%$ of deviations, mostly because of the simplified temperature field assumptions (Eqs. 27 and 28). It should be noted that traditional, relatively slow solidification in non-RSP processes is expected to result in narrower margins of size prediction error because of lower cooling and therefor nucleation and dendrite fragmentation rates. On the contrary, wider variation ranges in crystallite size estimates are anticipated in more complex initiation cases, such as in UDS droplets partially solidifying in flight, and promoting heterogeneous nucleation and dendrite breakup internally in the bulk upon deposition and cooling. The same applies to cases with more pronounced growth confinement, e.g., in RSP via spray forming into cooled molds of complex geometry, because of

the resulting complicated, non-uniform temperature field, with large differential thermal terms through the diversified geometry and boundary conditions.

6 Conclusions

Metal droplet sprays have been considered for application in rapid prototyping/additive manufacturing processes in this past decade [47–50]. This research introduces a simple yet comprehensive solidification model for crystallite size, based on a classical nucleation and dendrite fragmentation formulation, and an additional description of growth confined by development of adjacent domains. This constrained growth is described on the basis of differential features of temperature distribution and cooling rates. The model parameters are calibrated, and their predictions are validated in three cases of simple, semi-analytically described thermal fields, offering valuable insights to the model implementation. These test cases concern oil quenching of spherical particles and deposition of planar and globular splats on a cooling substrate. The model estimates are compared with experimental measurements of crystal domain size on solidified microstructures, with a prediction error of the constrained growth description within $\pm 10\%$. This could be further reduced with more accurate computational modeling of the dynamic thermo-fluid distributions during solidification, especially in more complex deposit geometries and process conditions.

Such an off-line numerical model, based, e.g., on finite-element methods, is useful for solidified material design and optimization of microstructure and its concomitant mechanical properties (e.g., grain boundary strengthening). A full parametric study of the model performance in such an additive manufacturing application [50], i.e., 3D printing/welding of arbitrarily shaped deposits by UDS droplets landing on a motion-controlled substrate, is currently underway. However, real-time control of RSP processes, i.e., in-process modulation of the melt thermal state, droplet dispensation frequency and flight height, in order to obtain desired crystallite sizes in the microstructure and material properties of the solidified deposits, requires feedback of such outputs during the process. Since both material structure and mechanical properties may be unavailable non-destructively during the short time span of RSP processes, substitute feedback of temperature measurements, e.g., by non-invasive infrared pyrometry on the droplet and/or splat surfaces, may need to be employed instead. In this closed-loop control scheme, a real-time process observer, i.e., a computationally efficient predictive model of the solidified structure from the measured temperature field, is essential for in-process regulation of the product quality. Therefore, further work is presently in progress towards use of the analytical formulation of the previous model as a real-time observer in RSP processes.

Funding information Y. Liao appreciates the financial support by startup funding from the Department of Mechanical Engineering at the University of Nevada, Reno.

References

- Hall E (1951) The deformation and ageing of mild steel: III discussion of results. *Proc Phys Soc Sect B* 64:747
- Petch N (1953) The cleavage strength of polycrystals. *J Iron Steel Inst* 174:25–28
- DeGarmo EP, Black JT, Kohser RA, Klamecki BE (1997) *Materials and process in manufacturing*. Prentice Hall, Upper Saddle River
- Lavernia EJ, Srivatsan TS (2010) The rapid solidification processing of materials: science, principles, technology, advances, and applications. *J Mater Sci* 45:287
- Steen PH, Karcher C (1997) Fluid mechanics of spin casting of metals. *Annu Rev Fluid Mech* 29:373–397
- Pekguleryuz M, Kaplan H, Neelameggham R, Hryn J, Nyberg E, Powell B, Cole G, Nie J (2002) Magnesium technology 2002, Part I: Primary production, environmental issues, high-temperature alloys. *JOM* 54:18–21
- Chun J-H, Passow CH (1993) Production of charged uniformly sized metal droplets, in, Google Patents
- Ranganathan R (2007) Liquid medium droplet deposition of copper, Doctor of Philosophy Dissertation, Northeastern University, Boston, MA
- Fortner W (1999) Construction of uniform droplet spray apparatus for mono-sized brass powder production. In: MS Thesis, Northeastern University
- Tuffile C (2001) Rapid epitaxial growth in mono-size droplet deposition of Sn and Sn-Pb alloys, Doctor of Philosophy Dissertation, Northeastern University, Boston, MA
- Passow CH, Chun J-H, Ando T (1993) Spray deposition of a Sn-40 Wt Pct Pb alloy with uniform droplets. *Metall Trans A* 24:1187–1193
- Pillai SK (2008) Processing of iron-based glass-forming alloys by the uniform-droplet spray process. In: Northeastern University
- Abesi Y (1999) Uniform droplet spraying of aluminium alloys, Master of Science Thesis. Northeastern University, Boston, MA
- Rayleigh L (1878) On the instability of jets. *Proc Lond Math Soc* 1: 4–13
- Ando T, Tuffile C, DiVenuti A, Chun J-H (1997) Calorimetric enthalpy measurement of traveling uniform droplets. *J Mater Synth Process(USA)* 5:31–37
- Chen C-A, Acquaviva P, Chun J-H, Ando T (1996) Effects of droplet thermal state on deposit microstructure in spray forming. *Scr Mater* 34:689–696
- Tuffile C, Ando T, Chun J-H (1998) Characterization of the in-flight solidification of Sn-Pb uniform droplets, *Solidification 1998*, Indianapolis, IN, 359–371
- Acquaviva P, Chen C-A, Chun J-H, Ando T (1997) Thermal modeling of deposit solidification in uniform droplet spray forming. *J Manuf Sci Eng* 119:332–340
- Lipton J, Kurz W, Trivedi R (1987) Rapid dendrite growth in undercooled alloys. *Acta Metall* 35:957–964
- Aziz MJ, Kaplan T (1988) Continuous growth-model for interface motion during alloy solidification. *Acta Metall* 36:2335–2347
- Boettinger WJ, Coriell SR, Trivedi R (1988) Application of dendritic growth theory to the interpretation of rapid solidification microstructure. In: *The Fourth Conference on Rapid Solidification Processing: Principles and Technology*, University of California Santa Barbara, pp 13–25
- DiVenuti AG, Ando T (1998) A free dendritic growth model accommodating curved phase boundaries and high Peclet number conditions. *Metall Mater Trans A* 29:3047–3056
- Galenko P, Phanikumar G, Funke O, Chernova L, Reutzel S, Kolbe M, Herlach D (2007) Dendritic solidification and fragmentation in undercooled Ni-Zr alloys. *Mater Sci Eng A* 449:649–653
- Karma A (1998) Model of grain refinement in solidification of undercooled melts. *Int J Non-Equilib Process(UK)* 11:201–233
- Tuffile CD, Ando T (2000) Epitaxial crystal growth in Sn and Sn-Pb alloys processed by mono-size droplet deposition. *J Mater Process Manu* 8:232–244
- Lu H, Ando T (2002) Modeling and characterization of the solidification of mono-size copper droplets. In: *The Proceedings of the JSME Materials and Processing Conference*, The Japan Society of Mechanical Engineers, pp 337–342
- Roy S, Ando T (2010) Nucleation kinetics and microstructure evolution of traveling ASTM F75 droplets. *Adv Eng Mater* 12:912–919
- Bialiauskaya V (2007) The nucleation kinetics of travelling Fe-17at% B droplets produced by the uniform-droplet spray process, Doctor of Philosophy Dissertation, Northeastern University, Boston, MA
- Zhang D (2007) Modeling and characterization of the solidification of mono-sized Mg-Al droplets produced by the uniform droplet spray process, in: MIE department, Northeastern University, Boston
- Fukuda H (2009) Droplet-based processing of magnesium alloys for the production of high-performance bulk materials. In: Northeastern University
- Carter GF (1979) *Principles of physical and chemical metallurgy*. American Society for Metals
- An J, Li RG, Chen CM, Xu Y, Chen X, Guo ZX, Liu YB (2007) Comparative studies on wear behaviour between as cast AZ91 and Mg97Zn1Y2 magnesium alloys. *Mater Sci Tech-Lond* 23:1208–1214
- Kawamura Y, Hayashi K, Inoue A, Masumoto T (2001) Rapidly solidified powder metallurgy Mg(97)Zn(1)Y(2) alloys with excellent tensile yield strength above 600 MPa. *Mater Trans* 42:1172–1176
- Matsumoto R, Otsu M, Yamasaki M, Mayama T, Utsunomiya H, Kawamura Y (2012) Application of mixture rule to finite element analysis for forging of cast Mg-Zn-Y alloys with long period stacking ordered structure. *Mat Sci Eng A-Struct* 548:75–82
- Villars P (1995) *Handbook of ternary alloy phase diagram*. The Material Information Society
- Wang BS, Liu YB, An J, Li RG, Su ZG, Su GH, Lu Y, Cao ZY (2008) Morphologies of microstructure in Mg97Zn1Y2 ribbon upon ageing at different temperatures. *Mater Trans* 49:1768–1774
- Yaghmazadeh M (2017) Evolution of core-shell structures in Al-Bi and Al-Sn alloy droplets. In: Northeastern University
- Gonzalez R, Woods R, Eddins S (2009) *Digital image processing using Matlab* Gatesmark Publishing. In: LLC
- Boettinger W (1988) Application of dendritic growth theory to the interpretation of rapid solidification microstructure, *Rapid Solidification Processing: Principles and Technology* 13
- Petrovic S, Robinson T, Judd RL (2004) Marangoni heat transfer in subcooled nucleate pool boiling. *Int J Heat Mass Transf* 47:5115–5128
- Porter D, Esterling K (1992) *Phase transformations, metals and alloys*, 2nd edn. Chapman & Hall, London
- Lu H, Ando T (2002) 513 Modeling and characterization of the solidification of mono-size copper droplets. In: *The Proceedings of the JSME Materials and Processing Conference (M&P)* 10.1, The Japan Society of Mechanical Engineers, pp 337–342
- Langer JS (1980) Instabilities and pattern formation in crystal growth. *Rev Mod Phys* 52:1

44. Connors K (1990) Introduction to chemical kinetics, Chemical Kinetics: the study of reaction rates in solution
45. Carslaw H, Jaeger J (1959) Conduction of heat in solids. Oxford Science Publications, Oxford
46. Wang P, Sun H, Wong PY, Fukuda H, Ando T (2012) Modeling of droplet-based processing for the production of high-performance particulate materials using the level set method. *Numer Heat Transfer Part A Appl* 61:401–416
47. Yin FL, Zhu S, Liu J, Liang YY (2012) Numerical simulation of molten metal droplet impinging in uniform droplet spray rapid prototyping. *Mater Sci Forum* 704-705:680–684
48. Qi LH, Chao YP, Luo J, Zhou JM, Hou XH, Li HJ (2012) A novel selection method of scanning step for fabricating metal components based on micro-droplet deposition manufacture. *Int J Mach Tool Manu* 56:50–58
49. Du J, Wang X, Bai H, Zhao GX, Zhang YB (2017) Numerical analysis of fused-coating metal additive manufacturing. *Int J Therm Sci* 114:342–351
50. Murr LE, Johnson WL (2017) 3D metal droplet printing development and advanced materials additive manufacturing. *J Mater Res Technol* 6:77–89

Publisher's note Springer Nature remains neutral with regard to jurisdictional claims in published maps and institutional affiliations.